Fluctuations in long-term seismicity in response to changing water levels along one of the Earth's largest lakes

Dongdong Yao[1], Yihe Huang[1], Liang Xue[2,3], Yuning Fu[2], Andrew Gronewold[1,4], Jeffrey L. Fox[5]*

1. Department of Earth and Environmental Sciences, College of Literature, Science, and Arts, University of Michigan.
2. School of Earth, Environment and Society, College of Arts and Sciences, Bowling Green State University.
3. Earth and Environmental Sciences, College of Arts and Sciences, Syracuse University.
4. School for Environment and Sustainability, University of Michigan.
5. Division of Geological Survey, Ohio Department of Natural Resources

*Corresponding author: Dr. Dongdong Yao (dongdony@umich.edu)

Abstract

The Great Lakes region is usually considered to be seismically inactive. However, earthquakes do occur around this region and may be related to stress changes caused by water level fluctuations. We perform a systematic template matching analysis of regional seismicity in 2013-2020 and calculate the Coulomb stress change caused by water loading. The new catalog reveals 20-40 M>0 earthquakes/year before 2019. The high seismicity rate in 2019 is dominated by active aftershocks following the M_L4.0 Ohio earthquake. Given the limited number of earthquakes, neither seasonal pattern nor obvious increasing trend of seismicity with fluctuating water levels can be established. However, we cannot rule out the role of increasing water level in reactivating the faults that host the 2019 Ohio earthquake sequence. The lake loading induced stress change is found to increase with water level at low effective friction coefficient, with maximum positive stress change of ~0.2 KPa ($\mu = 0.2$).

Plain Language Summary

Is the Great Lakes region seismically inactive? What might contribute to fault reactivation in this region? Is it just a coincidence that the 2019 M_L4.0 earthquake occurred during the high water level condition? Could the recent dramatic increase in lake water level have reactivated local faults and cause hazardous earthquakes? In this study, we conduct the first systematic long-term (2013-2020) seismicity monitoring around the southern Great Lakes and present an unprecedented complete catalog with many previously missing earthquakes. A nearly constant earthquake rate of ~20–40 earthquakes/year is observed before the occurrence of the 2019 M_L4.0 earthquake. We test whether the fluctuation of surface water level could impact the preexisting fault in this region. The surface loading-induced stress change is found to increase with the rise of water

level at low effective friction coefficient, with maximum positive stress change of ~0.2 KPa ($\mu = 0.2$).

Highlights

1. We obtain a more complete earthquake catalog by increasing the number of detected events near Lake Erie from 27 to 437 in 2013-2020.

2. Water loading-induced Coulomb stress change depends on fault friction and increases with water level for small friction coefficient.

3. Fault reactivation around the southern Great Lakes could be related to increasing water levels.

1. Introduction

Similar to other stable continental regions east of Rocky Mountains, the North American Laurentian Great Lakes, which collectively constitute the largest surface freshwater body on Earth, have been generally believed to be seismically inactive (Wheeler et al., 2003). The formation of the Great Lakes is a combined effect of glacial retreat and isostatic uplift, together with repeated scour and erosion of the bedrock beginning as early as ~2.4 Ma (Larson and Schaetzl, 2001). Contradicted by the large glacial isostatic adjustment (GIA) controlled strain inferred from GPS observations, $M_W \geq 5.0$ earthquakes are rarely reported around the Great Lakes (Kreemer et al., 2018). However, the constant occurrence of M>2 earthquakes in this region remains poorly understood and makes the Great Lakes a natural laboratory to understand how preexisting faults become activated.

Water levels on the Laurentian Great lakes have been recorded for over a century and, throughout that time period, have fluctuated across both seasonal (i.e., monthly) and annual scales (Gronewold et al., 2013; Lenters, 2001). Water levels during the 1960s, for example, reached record lows across much of the Great Lakes. Water levels then rose steadily into the 1980s, when they hit record highs. Importantly, the overall water level range across each of the Great Lakes is on the order of 1.5 to 2.0 meters. Over the past two decades, water level fluctuations across the Great Lakes have followed a distinct pattern that represents a departure from the previous historical period. Specifically, water levels on the Great Lakes were remarkably invariant from 1998 to 2013, a period when the hydrologic cycle was dominated by above-average lake surface temperatures and lake evaporation (Assel, 1998; Assel et al., 2004). In 2014, however, water levels across the Great lakes surged in response to extraordinary precipitation (Gronewold et al., 2016). The period of water level change on the Great Lakes from 2014 to 2021, in fact, represents the fastest rate of water level increase across the Great Lakes in recorded history (Gronewold et al., 2021).

Interestingly, despite the research on the changes in the hydrologic cycle of the past decade, little attention has been paid to the time coincidence between increasing water levels and elevated seismicity rates observed around the southern Great Lakes since 2010. Studies have suggested that the enhanced seismicity

could be attributed to wastewater injection and hydraulic fracturing (Brudzinski and Kozłowska, 2019). The so-called injection-induced earthquakes were recorded in different regions of eastern Ohio, including Ashtabula (Seeber et al., 2004), Youngstown (Kim, 2013; Holtkamp et al., 2013; Skoumal et al., 2014), Harrison county (Friberg et al., 2014; Skoumal et al., 2015a; Friberg et al., 2018; Kozłowska, 2018), Southern Trumbull county (Skoumal et al., 2015b), Poland Township (Skoumal et al., 2015c), as well as several isolated locations (Skoumal et al., 2015a). Besides fluid injection and hydraulic fracturing, the changes in the surface loading of natural water systems, including lakes and reservoirs, have been proposed to affect critically stressed faults and trigger earthquakes, such as the western branch of the East Africa Rift system (Xue et al., 2020) and reservoirs located in Koyna, Nurek and Aswan (Simpson et al., 2018, etc.), despite the fact that the associated stress changes are orders of magnitudes smaller.

On June 10, 2019, a M_L4.0 earthquake occurred in Lake County just offshore of Lake Erie. The earthquake was widely felt in regions up to 100 km away. It was preceded by several foreshocks, and followed by active aftershocks (Yao et al., 2021). The relative location result showed an ESE-WNW striking fault plane (a strike of N100°E), which is similar to strikes of Highlandtown, Smith Township, Suffield and Arkon faults to the south (Baranoski, 2013). This earthquake sequence exhibits a classic Gutenberg-Richter distribution, indicating that the associated faulting system can effectively transfer fault stress. In addition to occurring near the end of a period of record-setting water level rise across the Great Lakes, this event coincided with the highest water level ever recorded on Lake Erie. This phenomenon raises the question of whether changes in water loading across the Great Lakes region play a role in reactivating pre-existing faults.

We answer this question by establishing a template matching earthquake catalog in the southern Great Lakes region during 2013–2020, calculating the elastic loading stress changes due to lake water mass variations, and investigating the possible relationship between seismicity and the Coulomb stress change caused by the lake water loading. The US Transportable Array (TA), together with the central and eastern US network (N4), provides continuous recordings for the application of template matching during our study period. We use reported earthquakes listed in the Advanced National Seismic System Comprehensive Earthquake Catalog (ComCat) as templates, and scan with continuous data to identify previously missing events. Newly matched events are further used as new templates to build a more complete catalog. We also use water level observations over the past decade to compute the resulting Coulomb stress changes on the fault with geometry inferred from focal mechanism solutions of the recent M_L4.0 earthquake. We aim to monitor the long-term seismicity pattern and gain new insights into the mechanisms of fault reactivation in the southern Great Lakes.

1. Method and Results

2.1 Earthquake Catalog

We choose 27 M_L1.5-4.0 earthquakes listed in the ComCat (Figure 1; Table S1) between 2013 and 2020 as templates. We bandpass filter (5–15 Hz) seismic data recorded by the nearest station M52A, manually pick P- and S-wave arrivals of template earthquakes, and apply a single-station matched filter technique (SS-MFT) to search for missing earthquakes. To avoid spurious detections, we use both P- and S-wave for all three components to scan through continuous data (Meng et al., 2018). A 5s-long window starting 1s before P- or S-wave arrival is selected as the candidate template window. We calculate the signal-to-noise ratio (SNR) for each template window as the ratio between the cumulative energy (sum of the squared amplitude) of the template window and the noise window (which is defined as a 5s-long window right before the P-wave window). Only those templates with SNR above 5.0 for at least 3 template windows are further used.

For each template, a daily cross-correlation (CC) function is calculated by cross-correlating a selected template window with its corresponding daily continuous trace by sliding one data point each time. After obtaining all CC functions, we stack them to obtain the stacked CC trace, and report a positive detection when the CC value is above the defined threshold (median value + 12 times the median absolute deviation of the CC trace). We then combine detections from all templates and remove duplicate ones. Newly detected events which satisfy the SNR threshold criteria for at least 3 template windows are used as additional templates for a new round of template matching. Beyond local earthquakes, events associated with surficial blasts are also observed (Figure 2). We manually identify blasts based on clear Rg waves (Kafka, 1990), and separate them into a non-earthquake template library. Moreover, we further avoid possible contaminations from surficial sources by applying a high-pass filter of 5–15 Hz (Figure 2; Figure S1). We obtain final detection results when no additional templates can be further used. Our detection results include a total number of 537 events. By visually confirming visible P- and S-wave arrivals, we obtain a catalog of 437 earthquakes (Figure 3; Table S2). This corresponds to 15 times more events (M_L 0.0-2.7) when compared to those listed in ComCat.

2.2 Clustering Analysis

To further understand the temporal behavior of earthquakes, we perform a clustering analysis based on the waveform similarity. Due to a sparse station distribution, the majority of earthquakes only have visible P- and S-wave arrivals on station M52A. We cross-correlate events using a 6s-long window starting 2s before the S-wave (filtered 5-15 Hz) recorded by the station M52A, and output event pairs with cross-correlation coefficients above 0.6 for all three channels or 0.7 for two channels. Event pairs are grouped into families using the Equivalency Class algorithm (Peng and Ben-Zion, 2005), which groups a new member into a family when it pairs with any member of the family. The result includes 37 clusters with 2–152 members (Figure S2), containing a total number of 257 events.

Among all earthquakes clustered, a main cluster with 152 earthquakes corre-

sponds to the sequence around the epicenter of the 2019 M_L4.0 earthquake. This cluster started with two M2.7 earthquakes on 02/28/2013 and 03/08/2013, and remained inactive with only 5 M1–type earthquakes until the occurrence of several foreshocks of the 2019 M_L4.0 earthquake, then followed by active aftershocks (Figure S3). We also find several isolated clusters activated during the examined time window. Among them, the cluster with the most members (12 earthquakes) exhibits two main swarms on 11/08/2014 and 02/06/2015 (Figure S4).

2.3 Absolute Location

We use waveform data recorded by stations within 2 degrees relative to epicenters for both tectonic earthquakes and blasts. We manually pick P- and S-wave arrivals and apply Hypoinverse to obtain the absolute locations. A minimum number of 4 stations are required to locate an event, and we test two different velocity models in this region: a modified Kim's model (Kim, 2013) in Figure 1 and Ruff's model (Ruff et al., 1993) in Figure S5. Beyond tectonic earthquakes, we also locate blasts as shown in Figure 2 (Table S3). There are four main clusters of earthquakes within Lake County, together with several isolated ones (Figure 1). Among them, cluster 1 mainly corresponds to the 2019 M_L4.0 Ohio sequence. We are also able to resolve two main sources of blasts: one associated with surficial quarry blasts in lower Ohio near Harrison county (Figure S5): and the other one located close to the epicentral region of the 1986 M5.0 Lake earthquake (Figure 1, Figure S6 & S7).

2.4 Coulomb Stress Calculation and Fault Reactivation

To further evaluate water loading-induced stress change on the fault that hosted the 2019 Ohio earthquake sequence, we use the static finite element code, Pylith (Aagaard et al., 2008), to resolve fault stress changes induced by water loading of Lake Erie. The fault geometry is derived from the SLU nodal plane of the 2019 Ohio mainshock with strike, dip, and rake as 100°, 65°, and 25° (http://www.eas.slu.edu/eqc/eqc_mt/MECH.NA/20190610145044/index.html; Last accessed: 07/2021). We construct a 700x500x100 km tetrahedral volume mesh with a cell size of 4km over the lake (Figure 4). We add time-variable surface water levels recorded from the tide gauge station 9063063 at Cleveland as traction on the surface of the mesh (Figure 1). The PREM model (Dziewonski and Anderson, 1981) is applied to assign the elastic properties of the mesh. We compute the time series of stress tensor using the total surface water mass load variation and calculate the normal, shear, and Coulomb stresses at seismogenic depth (3 km) on the fault plane.

The stress change induced by lake water loading presents a strong seasonality (Figure 4). For our fault geometry, normal tensile stress rises when the lake level is low in winter, while shear stress presents an opposite behavior and increases with the rise of the lake level (Figure S8). Therefore, the Coulomb stress change is dependent on and sensitive to the value of the effective friction coefficient, μ, as shown in the sensitivity analysis (Figure 4). The Coulomb stress change

would increase with the rise of lake water when μ<=0.3, indicating a favorable condition for the occurrence of local seismicity, whereas a larger μ would lead to decreasing Coulomb stress change with elevating lake level and prohibits the fault from rupturing. Although μ of 0.4 is widely applied in calculations of Coulomb stress changes to minimize uncertainty (Stein et al., 1992; King et al., 1994; Toda et al., 2011), a smaller μ value is plausible in this region due to the potential existence of trapped fault fluids (Stein, 1999) given a shallow focal depth (Yao et al., 2021) and proximity to the Lake. Previous studies also suggest a smaller frictional coefficient for strike-slip faults (Xiong et al., 2010; Toda and Stein, 2002). When choosing a μ of 0.2, the annual peak to peak normal, shear, and Coulomb stress are ~1.5, 0.5, and 0.2 kPa, respectively (Figure S8). Such influence of μ on the magnitude of Coulomb stress changes is also supported by previous studies. For example, the Coulomb stress at the epicenter of the Christchurch earthquake were 0.95, 0.44, and -0.08 bar with μ of 0, 0.4, and 0.8, respectively (Zhan et al., 2011).

2.5 Correlation analysis

We perform a linear regression between earthquake rate and water level data. Monthly earthquake rate is calculated as the number of earthquakes per month between 2013 and 2020. We obtain the monthly water level recording from station 9063063, and derive the rate of change in monthly water level. The low R^2 values indicate no conclusive correlation can be established between earthquake rate and water level or water level change rate (Figure 3). A similar conclusion is drawn by excluding earthquakes in cluster 2 and 3 (Figure 1) further away from the shore of Lake Erie based on absolute locations in section 2.3 (Figure S9), where water injection could be an alternative origin for earthquakes (e.g., Nicholson et al., 1988). Likewise, we cannot establish the relationship between total seismic moment per month, which is dominated by seismic moments of relatively large events, and water level or water level change rate (Figure S10). Hence, we do not observe either a clear seasonal variation or increasing seismicity rate associated with seasonally fluctuating and increasing water levels, although we find a peak in seismicity activity during high water level season in 2019, as well as more earthquakes when water level changes rapidly (decreasing water level in late 2014 and early 2015, as well as increasing water level in early 2017). The lack of statistical relationship is likely due to a limited number of earthquakes in our catalog despite having 15 times more events.

1. Discussion and Conclusion

3.1 Water loading vs. earthquakes

It has been known that stress change induced by surface water load can induce earthquakes (McGarr et al., 2002). These include seismicity associated with impounded reservoirs (Gupta and Rastogi, 1976; Gupta, 1985; Kebeasy et al., 1987; Simpson et al., 1990; Simpson and Negmatullaev, 1981; Carder, 1970; Roeloffs, 1988; Simpson et al., 2018) or modulated by seasonal variations in water levels of hydrological systems, including surface lakes (Pandey and Chadha,

2003; Xue et al., 2020), aquifers (Chaussard et al., 2014; Hu and Burgmann, 2020), groundwater (Amos et al., 2014; Johnson et al., 2017; Chaussard et al., 2017; Wang et al., 2019). The underlying mechanism of lake-induced seismicity can involve interactions between shear stress, normal stress and pore pressure. Xue et al. (2020) observed a correlation between seismicity and Coulomb stress induced by water loading without obvious time lags in the western branch of the East African Rift system. In comparison, Simpson et al. (2018) summarized that reservoir triggered seismicity is significantly influenced by the change rate of reservoir water level. Moreover, Gupta (1983) showed that seismicity tends to correlate with periods of high water level and large rates of increase in water level at Koyna.

In our study, we observe no temporal correlation between seismicity and water level before the 2019 Ohio sequence. Besides the limited number of earthquakes in the catalog, this could also be due to the fact that the lake-induced stress change from either seasonal variation (less than 0.5 m) or long-term increase (~1 m) in water level is orders of magnitude smaller than from water impoundment in larger water reservoirs (Simpson et al., 2018), where the water level can fluctuate in the order of tens to hundreds of meters. Unlike the case reported in the western branch of the East African Rift system (Xue et al., 2020), the Great Lakes is also much less tectonically active. Hence, the modulation of seasonally fluctuating water level on local seismicity is less obvious compared to regions with active tectonics and critically stressed faults. Given the fact that stress change on the order of several hundred pascals can modulate seismicity (Xue et al., 2020), whether and how the increasing water level contributes to the occurrence of the 2019 Ohio earthquake remains an open question. Future research directions include extending the time window to early periods and monitoring the local activity by denser instrumentations.

3.2 Nearby natural/induced earthquakes

The area to the southern Great Lakes near the shore of Lake Erie has hosted both injection-induced and tectonic earthquakes. Skoumal et al. (2015a) suggested that earthquakes within Lake County likely have natural origins due to the relatively large distances (greater than 10 km) between earthquake epicenters and active wastewater disposal wells. In comparison, Seeber et al. (2004) found that the persistent earthquake sequence in Ashtabula, Ohio, was triggered by fluid injection. Nicholson et al. (1988) pointed out that the triggering of the 1986 M_L5.0 earthquake by well activities cannot be ruled out. In this study, we note that two main clusters 2 and 3 (Figure 1) located in the vicinity of the 1986 earthquake and operating wells might be potentially caused by nearby well activities. More intriguingly, the 1986 earthquake also happened during another period of recorded high water levels across the Great Lakes (Figure S11). However, due to a large distance relative to Lake Erie, it would be difficult to evaluate the impact of the lake-induced stress change on triggering the 1986 earthquake.

Although no M>4 earthquakes have occurred in the study region since the

1986 M_L5.0 earthquake, M>3 earthquakes occurred regularly. For example, an active sequence of earthquakes occurred within 20 km to the northeast of the 2019 Ohio earthquake between 2006 and 2010. Their locations suggest a SES-NWN striking fault beneath Lake Erie (Figure 1). Given the distribution of offshore hypocenters, these events are more likely natural. However, whether those earthquakes occurred on the same fault as the ruptured fault plane of the 2019 Ohio earthquake or a nearby parallel fault remains enigmatic.

3.3 Anthropogenic noises and limitations

We note that the tectonic earthquake signal in this study area could be contaminated by events of anthropogenic origins, which generally begin with high frequencies and follow by long-period surface waves. Those anthropogenic events exhibit regular occurrence patterns since they are associated with either mining or surface quarry blast activities, and normally occur during work hours (10:00 to 16:00 of the day) of weekdays (Figure S12). We also observe events similar to the previously reported Short Duration Events (SDEs; Figure S13). SDEs were observed by ocean bottom seismometers worldwide (Tary et al., 2012; Batsi et al., 2019; Hilmo and Wilcock, 2020; etc.), and were attributed to either biological interactions or associated with gas bubble movement in seafloor sediments. Although we are not certain about the origins of those SDE-like events, the aforementioned causes cannot explain those observed at station M52A located in a farm plain.

Our attempt to build the catalog strongly depends on the starting catalog, which could inevitably be bottlenecked by inadequate coverage of the stations. Since the SS-MFT enforces a relatively weaker constraint on the location of a match event when compared to network-based MFT, we are able to identify new earthquakes with comparable epicentral distances instead of in the vicinity of templates. However, it is hard to resolve the absolute locations of relatively small events with high confidence levels. Despite the fact that we cannot fully recover hidden events in regions without any template, we are confident that we can detect any possible events near existing templates. Hence, our conclusions hold robust for regions with relatively good coverage of templates. Further analysis based on continuous recording of station M52A can take advantage of the catalog obtained in this study and incorporate more advanced machine learning techniques to automatically detect unknown events, which would be the subject of our future work.

Acknowledgements

Seismic data utilized in this study are requested and downloaded from the Incorporated Research Institutions for Seismology Data Management Center (TA.M52A: https://ds.iris.edu/mda/TA/M52A/?starttime=2013-01-17&endtime=2014-10-28 & N4.M52A: https://ds.iris.edu/mda/N4/M52A/?starttime=2014-10-28&endtime=2599-12-31) and processed with Seismic Analysis Code (SAC). Water level data from stations around Lake Erie of Great Lakes are obtained from NOAA Tides & Currents (e.g., monthly water level

data from station 9063063 Cleveland, OH can be downloaded via the link: https://tidesandcurrents.noaa.gov/waterlevels.html?id=9063063&units=metric&bdate=20130101&edate=20201231&timezone=LST/LDT&datum=IGLD&interval=m&action=data; Last accessed: June 2021). Figures were created using Generic Mapping Tools (GMT) and MATLAB. DY and YH are supported by the National Science Foundation grant 1943742. YF and LX are funded by the NASA Earth Surface and Interior grants 80NSSC19K0361 and NNX17AE01G. Data products are archived in Table S1-S3.

Reference

Aagaard, B., Williams, C., & Knepley, M. (2008). PyLith: A finite-element code for modeling quasi-static and dynamic crustal deformation. Eos, Transactions American Geophysical Union, 89(53).

Amos, C. B., Audet, P., Hammond, W. C., Bürgmann, R., Johanson, I. A., & Blewitt, G. (2014). Uplift and seismicity driven by groundwater depletion in central California. *Nature*, 509(7501), 483– 486. https://doi.org/10.1038/nature13275.

Argus, D. F., Ratliff, B., DeMets, C., Borsa, A. A., Wiese, D. N., Blewitt, G., et al. (2020). Rise of Great Lakes surface water, sinking of the upper Midwest of the United States, and viscous collapse of the forebulge of the former Laurentide ice sheet. Journal of Geophysical Research: Solid Earth, 125(9), e2020JB019739.

Assel, R. A. (1998). The 1997 ENSO event and implications for North American Laurentian Great Lakes winter severity and ice cover. Geophysical Research Letters, 25(7), 1031–1033.

Assel, R. A., Quinn, F. H., & Sellinger, C. E. (2004). Hydroclimatic factors of the recent record drop in Laurentian Great Lakes water levels. Bulletin of the American Meteorological Society, 85(8), 1143–1151.

Baranoski, M. T. (2013). Structure contour map on the Precambrian unconformity surface in Ohio and related basement features (ver. 2.0), Ohio Department of Natural Resources, Division of Geological Survey Map PG-23, scale 1:500,000, 17 pp.

Batsi, E., Tsang-Hin-Sun, E., Klingelhoefer, F., Bayrakci, G., Chang, E. T. Y., Lin, J., et al. (2019). Nonseismic signals in the ocean: Indicators of deep sea and seafloor processes on ocean-bottom seismometer data. Geochemistry, Geophysics, Geosystems, 20, 3882–3900.

https://doi.org/10.1029/2019GC008349.

Brudzinski, M. R., & Kozłowska, M. (2019). Seismicity induced by hydraulic fracturing and wastewater disposal in the Appalachian Basin, USA: A review. Acta Geophysica, 67(1), 351–364. https://doi.org/10.1007/s11600-019-00249-7.

Carder, D.S. (1970). Reservoir loading and local earthquakes, in *Engineering*

Seismology - the works of man in Engineering Geology Case Histories (Ed. W.M. Adams), Geol. Soc. Amer. 8.

Chaussard, E., Burgmann, R., Shirzaei,M., Fielding, E. J., & Baker, B. (2014). Predictability of hydraulic head changes and characterization of aquifer-system and fault properties from InSAR-derived ground deformation. Journal of Geophysical Research: Solid Earth, 119, 6572–6590. https://doi.org/10.1002/2014JB011266.

Chaussard, E., Milillo, P., Bürgmann, R., Perissin, D., Fielding, E. J., & Baker, B. (2017). Remote sensing of ground deformation for monitoring groundwater management practices: Application to the Santa Clara Valley during the 2012–2015 California drought. Journal of Geophysical Research: Solid Earth, 122, 8566–8582. https://doi.org/10.1002/2017JB014676.

Dziewonski, A. M., & Anderson, D. L. (1981). Preliminary reference Earth model. Physics of the Earth and Planetary Interiors, 25(4), 297–356. https//doi.org/10.1016/0031-9201(81)90046-7.

Friberg, P. A., G. M. Besana-Ostmanb, and I. Dricker (2014), Characterization of an earthquake sequence triggered by hydraulic fracturing in Harrison County, Ohio, Seismol. Res. Lett., doi:10.1785/0220140127.

Friberg, P., Brudzinski, M. R., Fasola, S., Kozłowska, M., Skoumal, R. (2018). Seismicity induced by hydraulic fracturing in Ohio in 2016: case study of the Conotton sequence in Harrison County. 36th General Assembly of the ESC abstract.

Gronewold, A. D., Fortin, V., Lofgren, B. M., Clites, A. H., Stow, C. A., & Quinn, F. H. (2013). Coasts, water levels, and climate change: A Great Lakes perspective. Climatic Change, 120(4), 697–711.

Gronewold, A. D., Bruxer, J., Durnford, D., Smith, J. P., Clites, A. H., Seglenieks, F., … Fortin, V. (2016). Hydrological drivers of record-setting water level rise on Earth's largest lake system. Water Resources Research, 52(5), 4026–4042.

Gronewold, A. D., Do, H. X., Mei, Y., & Stow, C. A. (2021). A tug-of-war within the hydrologic cycle of a continental freshwater basin. Geophysical Research Letters, 48(4), e2020GL090374. https://doi.org/10.1029/2020GL090374.

Gupta, H. K., & Rastogi, B. K. (1976). Dams and earthquakes, (p. 227). Amsterdam: Elsevier.

Gupta, H. K. (1983), Induced seismicity hazard mitigation through water level manipulation: A suggestion, Bull. Seismol. Soc. Am., 73, 679–682.

Gupta, H. K. (1985), The present status of reservoir induced seismicity investigations with special emphasis on Koyna earthquakes, Tectonophysics, 118(3–4), 257–279.

Hilmo, R., & Wilcock, W. S. D. (2020). Physical sources of high-frequency seismic noise on Cascadia Initiative ocean bottom seismometers. *Geochemistry, Geophysics, Geosystems*, 21, e2020GC009085. https://doi.org/10.1029/2020GC009085.

Holtkamp, S. G., Brudzinski, M. R., & Currie, B. S. (2015). Regional detection and monitoring of injection-induced seismicity: Application to the 2010–2012 Youngstown, Ohio, seismic sequence. AAPG Bulletin, 99(9), 1671–1688. https://doi.org/10.1306/03311513194.

Hu, X., & Bürgmann, R. (2020). Aquifer deformation and active faulting in Salt Lake Valley, Utah, USA. Earth and Planetary Science Letters, 547, 116471. https://doi.org/10.1016/j.epsl.2020.116471.

Johnson, C. W., Fu, Y., & Bürgmann, R. (2017). Stress models of the annual hydrospheric, atmospheric, thermal, and tidal loading cycles on California faults: Perturbation of background stress and changes in seismicity. Journal of Geophysical Research: Solid Earth, 122, 10–605. https://doi.org/10.1002/2017JB014778.

Kafka, A. L. (1990), Rg as a depth discriminant for earthquakes and explosions: A case study in New England, Bull. Seismol. Soc. Am., 80(2), 373–394.

Kebeasy, R. M., Maamoun, M., Ibrahim, E., Megahed, A., Simpson, D. W., & Leith, W. S. (1987). Earthquake studies at Aswan reservoir, *J. Geodyn.*, **7**, 173–193, doi:10.1016/0264-3707(87)90003-2.

Kim, W.-Y. (2013). Induced seismicity associated with fluid injection into a deep well in Youngstown, Ohio. Journal of Geophysical Research: Solid Earth, 118, 3506–3518. https://doi.org/10.1002/jgrb.50247.

King, G. C. P., Stein, R. S., & Lin, J. (1994). Static stress changes and the triggering of earthquakes. Bulletin of the Seismological Society of America, 84, 935–953.

Kozłowska, M., Brudzinski, M. R., Friberg, P., Skoumal, R. J., Baxter, N. D., & Currie, B. S. (2018). Maturity of nearby faults influences seismic hazard from hydraulic fracturing. *Proceedings of the National Academy of Sciences*, 115(8), E1720–E1729. https://doi.org/10.1073/pnas.1715284115.

Kreemer, C., Hammond, W. C., & Blewitt, G. (2018). A robust estimation of the 3-D intraplate deformation of the North American plate from GPS. Journal of Geophysical Research: Solid Earth, 123, 4388–4412. https://doi.org/10.1029/2017JB015257.

Larson, G., and R. Schaetzl (2001), Origin and evolution of the Great Lakes, J. Great Lakes Res., 27, 518-546.

Lenters, J. D. (2001). Long-term trends in the seasonal cycle of Great Lakes water levels. Journal of Great Lakes Research, 27(3), 342–353.

Meng, X., Yang, H., & Peng, Z. (2018). Foreshocks, b value map, and aftershock

triggering for the 2011 Mw 5.7 Virginia earthquake. Journal of Geophysical Research: Solid Earth, 123, 5082–5098. https://doi.org/10.1029/2017JB015136.

McGarr, A., Simpson, D., & Seeber, L. (2002). Case histories of induced and triggered seismicity. International Geophysics Series, 81(A), 647–664.

Nicholson, C., E. Roeloffs, and R. L.Wesson (1988), The Northeastern Ohio earthquake of 31 January 1986: Was it induced?, Bull. Seismol. Soc. Am., 78(1), 188–217.

Pandey, A. P., & Chadha, R. K. (2003). Surface loading and triggered earthquakes in the Koyna–Warna region, western India. Physics of the Earth and Planetary Interiors, 139(3-4), 207–223.

Peng, Z., and Y. Ben-Zion (2005), Spatiotemporal variations of crustal anisotropy from similar events in aftershocks of the 1999 M7.4 İzmit and M7.1 Düzce, Turkey, earthquake sequences, Geophys. J. Int., 160, 1027–1043, doi:10.1111/j.1365-246X.2005.02569.x.

Roeloffs, E. (1988). Fault stability changes induced beneath a reservoir with cyclic variations in water level. Journal of Geophysical Research, 93(B3), 2107–2124. https://doi.org/10.1029/JB093iB03p02107.

Ruff, L., R. LaForge, R. Thorson, T. Wagner, and F. Goudaen (1994). Geophysical investigations of the western Ohio–Indiana region, NUREG/CR–3145-Vol.10, United States, available at https://www.osti.gov/servlets/purl/10125214 (last accessed August 2020).

Seeber, L., J. Armbruster, and W. Y. Kim (2004), A fluid-injection triggered earthquake sequence in Ashtabula, Ohio: Implications for seismogenesis in stable continental regions, Bull. Seismol. Soc. Am., 94, 76–87.

Simpson, D. W., & Negmatoullaev, S. K. (1981). Induced seismicity at Nurek reservoir, Tajikistan,. USSR, Bull. Seismol. Soc. Am., 71, 1561-1586.

Simpson, D. W., A. A. Gharib, and R. M. Kebeasy (1990), Induced seismicity and changes in water level at Aswan reservoir, Egypt, Gerlands Beitr. Geophys. Leipzig, 99, 191–204.

Simpson, D.W., Stachnik, J.C. & Negmatoullaev, S.K. (2018). Rate of change in lake level and its impact on reservoir triggered seismicity, Bull. seism. Soc. Am., 108(5B), 2943–2954.

Skoumal, R. J., M. R. Brudzinski, B. S. Currie, and J. Levy (2014), Optimizing multi-station earthquake template matching through re-examination of the Youngstown, Ohio, sequence, Earth Plant. Sci. Lett., 405, 274–280, doi:10.1016/j.epsl.2014.08.033.

Skoumal, R. J., Brudzinski, M. R., & Currie, B. S. (2015a). Distinguishing induced seismicity from natural seismicity in Ohio: Demonstrating the utility of waveform template matching. Journal of Geophysical Research: Solid Earth, 120, 6284–6296. https://doi.org/10.1002/

2015JB012265.

Skoumal, R. J., M. R. Brudrinski, and B. S. Currie (2015b), Microseismicity induced by deep wastewater injection in Southern Trumbull County, Ohio, Seismol. Res. Lett., 86, 1–9, doi:10.1785/0220150055.

Skoumal, R. J., M. R. Brudzinski, and B. S. Currie (2015c), Induced earthquakes during hydraulic fracturing in Poland Township, Ohio, Bull. Seismol. Soc. Am., 105(1), 189–197, doi:10.1785/0120140168.

Stein, R. S., King, G. C. P., & Lin, J. (1992). Change in failure stress on the southern San Andreas fault system caused by the 1992 magnitude = 7.4 Landers earthquake. Science, 258(5086), 1328–1332. https://doi.org/10.1126/science.258.5086.1328.

Stein, R. S. (1999). The role of stress transfer in earthquake occurrence. *Nature*, 402, 605–609. https://doi.org/10.1038/45144.

Tary, J. B., Géli, L., Guennou, C., Henry, P., Sultan, N., Çağatay, N., & Vidal, V. (2012). Microevents produced by gas migration and expulsion at the seabed: A study based on sea bottom recordings from the Sea of Marmara: Microevents produced by gas migration. Geophysical Journal International, 190(2), 993–1007. https://doi.org/10.1111/j.1365-246X.2012.05533.x.

Toda, S., & Stein, R. S. (2002). Response of the San Andreas fault to the 1983 Coalinga-Nuñez earthquakes: An application of interaction-based probabilities for Parkfield. *Journal of Geophysical Research*, 107(B6), 2126. https://doi.org/10.1029/2001JB000172.

Toda, S., R. S. Stein, V. Sevilgen, and J. Lin (2011), Coulomb 3.3 Graphic-rich deformation and stress-change software for earthquake, tectonic, and volcano research and teaching—User guide: U.S. Geol. Surv. Open File Rep., vol. 63, pp. 2011–1060. [Available at http://pubs. usgs.

gov/of/2011/1060/.]

Wang, S., Xu, W., Xu, C., Yin, Z., Bürgmann, R., Liu, L., & Jiang, G. (2019). Changes in groundwater level possibly encourage shallow earthquakes in central Australia: The 2016 Petermann Ranges earthquake. Geophysical Research Letters, 46, 3189–3198. https://doi.org/

10.1029/2018GL080510.

Wheeler, R. C. (2003). Tectonic summaries for web-served earthquake responses, southeastern North America, *U.S. Geol. Surv. Open-File Rept. 03-343*, 27 pp.

Xiong, X., Shan, B., Zheng, Y., & Wang, R. (2010). Stress transfer and its implication for earthquake hazard on the Kunlun Fault, Tibet. *Tectonophysics*, 482, 216–225.

Xue, L., Johnson, C. W., Fu, Y., & Bürgmann, R. (2020). Seasonal seismicity in the Western Branch of the East African Rift System. Geophysical Research

Letters, 47(6), 1–9. https://doi.org/10.1029/2019GL085882.

Yao, D., Huang, Y., & Fox, J. L. (2021). New Insights into the Lake Erie Fault System from the 2019 ML 4.0 Ohio Earthquake Sequence. *Seismological Research Letters*, 92(4), 2531–2539. doi: https://doi.org/10.1785/0220200335.

Zhan, Z. W., B. K. Jin, S. J. Wei, & R. W. Graves (2011). Coulomb stress change sensitivity due to variability in mainshock source models and receiving fault parameters: A case study of the 2010–2011 Christchurch, New Zealand, earthquakes, Seismol. Res. Lett., 82(6), 800-814, doi:10.1785/gssrl.82.6.800.

Figure Captions:

Figure 1. Map showing the study region. a) Red filled stars are 27 catalogued earthquakes used in this study, while filled black stars are nearby seismicity (2013-2020). Gray triangles are nearby stations, while the continuously recording station M52A is shown with the blue triangle. Cyan squares and triangles are locations of induced earthquakes by hydraulic fracturing and wastewater injection. L – 1986 M5.0 Lake earthquake; A – Ashtabula sequences (1987-2003). Top left inset locates the study region within the North American Laurentian Great Lakes, while the water level recording (Cleveland station 9063063) between 2005 and 2020 is plotted in the top right inset. b) Earthquake absolute locations (filled red stars) within the dashed box outlined in panel a), together with background seismicity between 1980 and 2013 (open stars) and nearby blasts (filled magenta stars). Four main clusters are labeled with numbers.

Figure 2. Different kinds of events detected through template matching. a) & b) The 2019 M_L4.0 Ohio mainshock. c) & d) A M2.6 aftershock. e) & f) The M3.4 Detroit earthquake. g) & h) Matched surficial quarry blast. i) and j) Matched mining blasts.

Figure 3. Earthquake detection result. a) Magnitude versus time. Red stars are 27 events listed in the ComCat, with bigger stars for M>3 earthquakes. Red open circles are additional templates, and black open circles are new detections. Black thick line shows the cumulative number of earthquakes. b) Earthquake monthly rate (black curve), relative water level data (RWL: red curve, set 174.5m as the reference zero water level), and change rate in monthly water level (blue curve). c) Linear regression between earthquake rate and water level (WL). The R^2 value is 0.007. d) Linear regression between earthquake rate and water level change rate (blue open circles) well as the absolute change rate (cyan filled squares). The corresponding R^2 values are 0.0001 and -0.001.

Figure 4. Finite element model mesh (a) and modelled Coulomb stress changes for different effective friction coefficients (μ) of 0.1-0.8 (b). We adopt PREM to assign the elastic properties of the mesh. The loading from Lake Erie is added on top of mesh as a boundary condition. The yellow dot represents the location of the modelled fault. The stress tensors are projected onto the target fault plane.

Figures

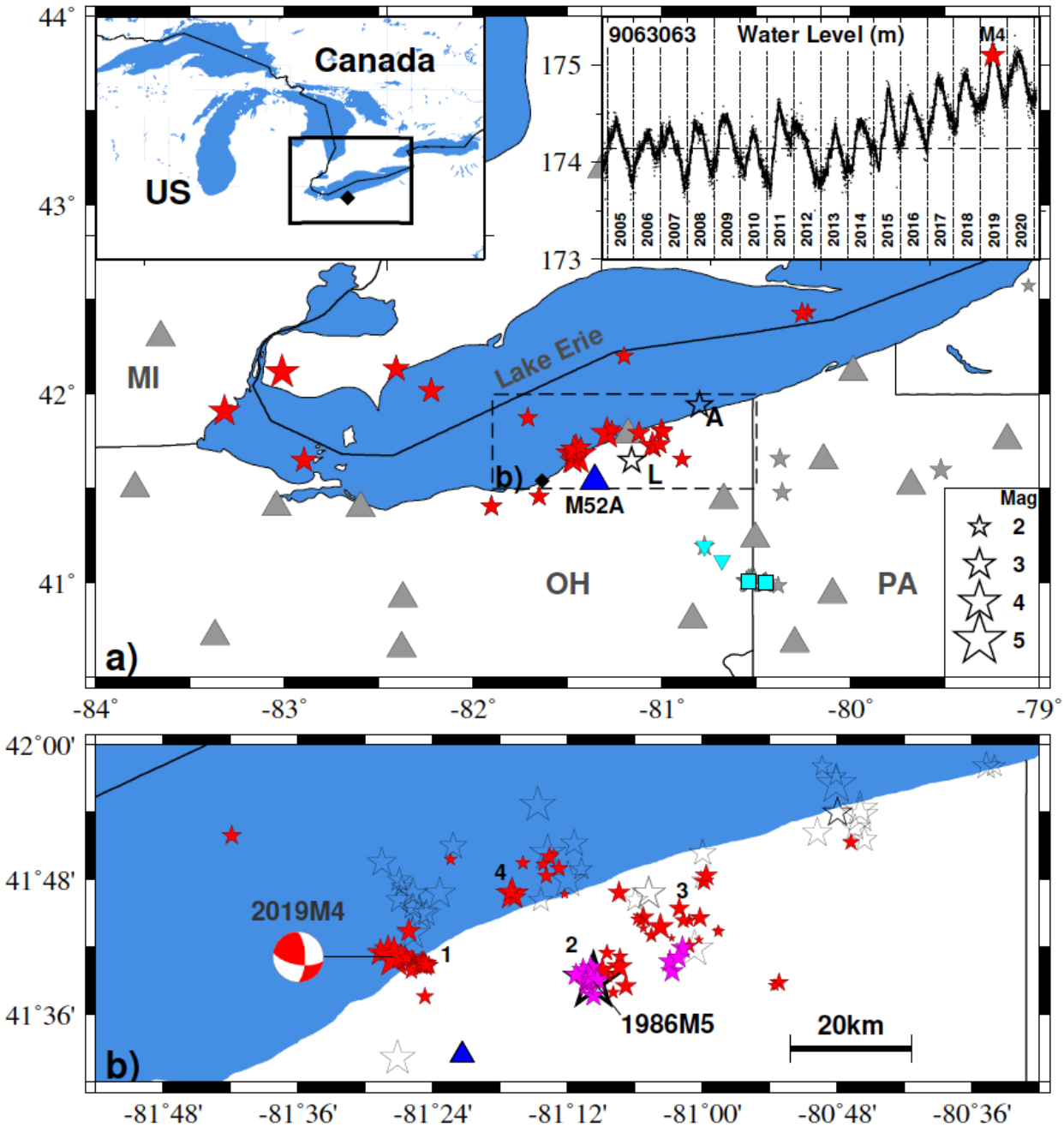

Figure 1. Map showing the study region. a) Red filled stars are 27 catalogued earthquakes used in this study, while filled black stars are nearby seismicity (2013-2020). Gray triangles are nearby stations, while the continuously record-

ing station M52A is shown with the blue triangle. Cyan squares and triangles are locations of induced earthquakes by hydraulic fracturing and wastewater injection. L – 1986 M5.0 Lake earthquake; A – Ashtabula sequences (1987-2003). Top left inset locates the study region within the North American Laurentian Great Lakes, while the water level recording (Cleveland station 9063063) between 2005 and 2020 is plotted in the top right inset. b) Earthquake absolute locations (filled red stars) within the dashed box outlined in panel a), together with background seismicity between 1980 and 2013 (open stars) and nearby blasts (filled magenta stars). Four main clusters are labeled with numbers.

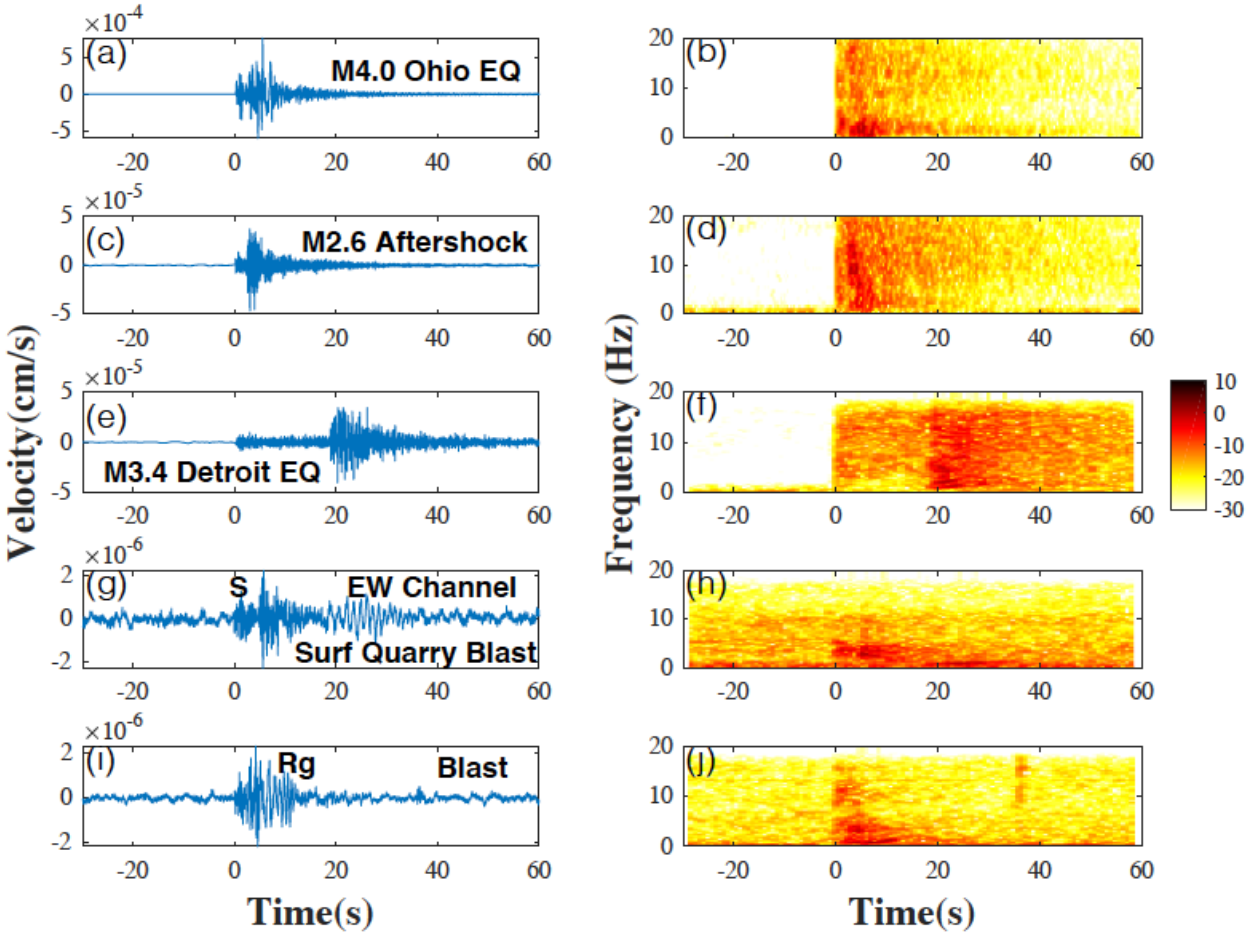

Figure 2. Different kinds of events detected through template matching. a) & b) The 2019 M_L4.0 Ohio mainshock. c) & d) A M2.6 aftershock. e) & f) The M3.4 Detroit earthquake. g) & h) Matched surficial quarry blast. i) and j) Matched mining blasts.

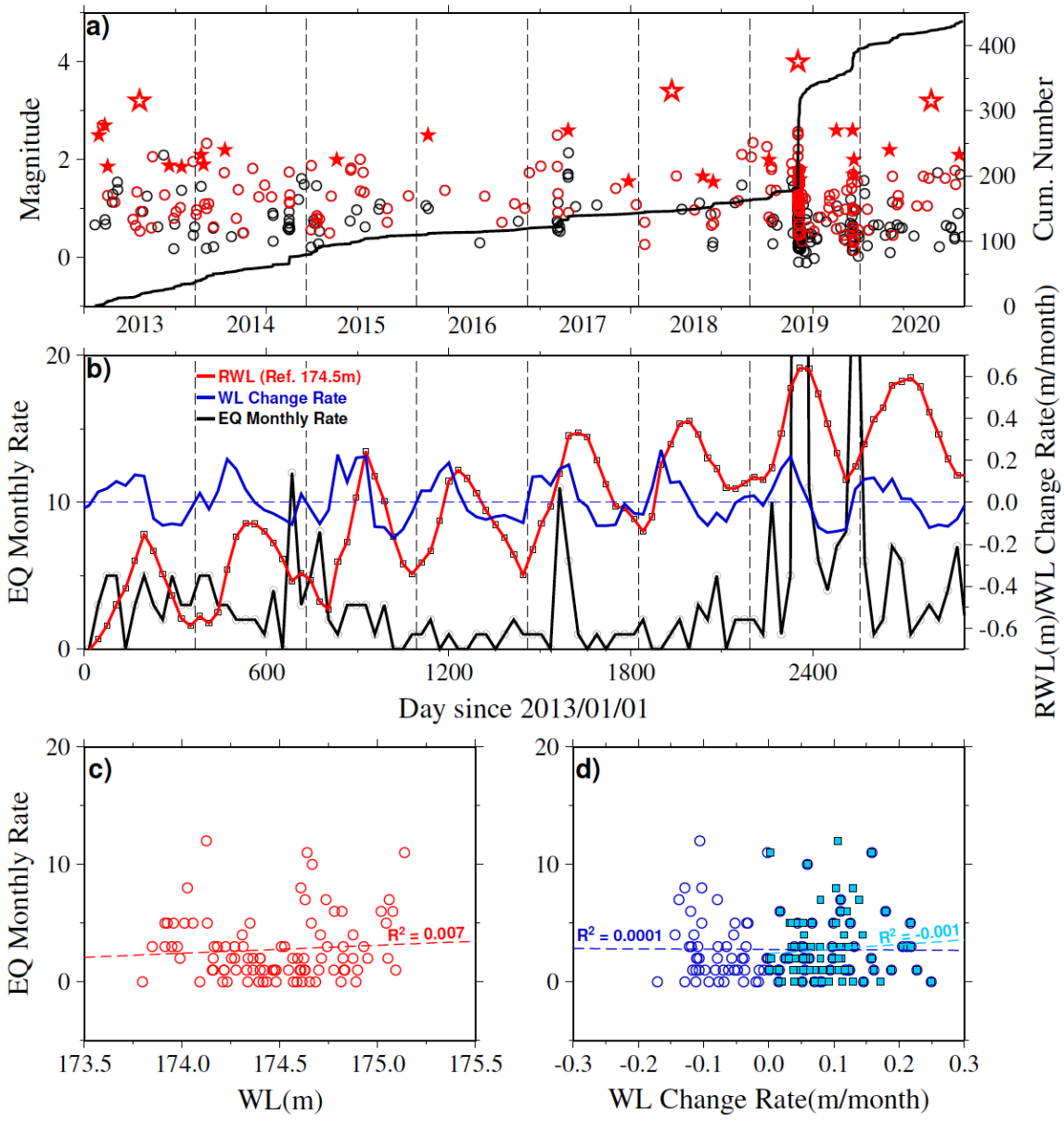

Figure 3. Earthquake detection result. a) Magnitude versus time. Red stars are 27 events listed in the ComCat, with bigger stars for M>3 earthquakes. Red open circles are additional templates, and black open circles are new detections. Black thick line shows the cumulative number of earthquakes. b) Earthquake monthly rate (black curve), relative water level data (RWL: red curve, set 174.5m as the reference zero water level), and change rate in monthly water level (blue curve). c) Linear regression between earthquake rate and wa-

ter level (WL). The R^2 value is 0.007. d) Linear regression between earthquake rate and water level change rate (blue open circles) well as the absolute change rate (cyan filled squares). The corresponding R^2 values are 0.0001 and -0.001.

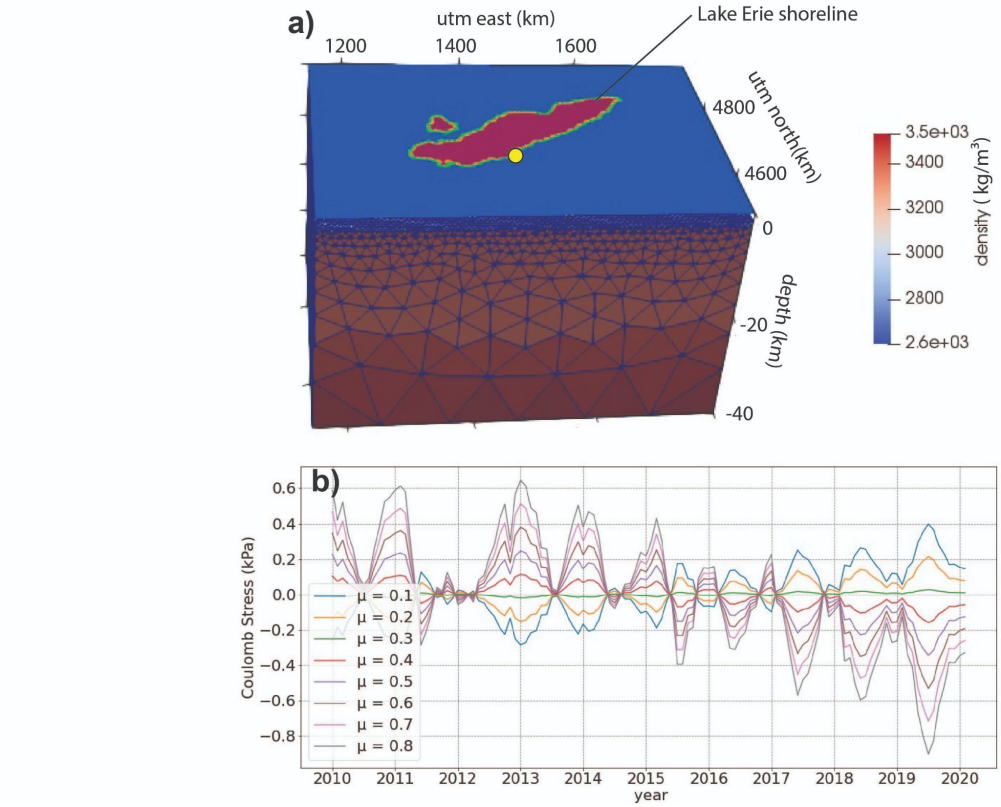

Figure 4. Finite element model mesh (a) and modelled Coulomb stress changes for different effective friction coefficients (μ) of 0.1-0.8 (b). We adopt PREM to assign the elastic properties of the mesh. The loading from Lake Erie is added on top of mesh as a boundary condition. The yellow dot represents the location of the modelled fault. The stress tensors are projected onto the target fault plane.